Left column (page 524)

Figure 5 | Diffuse scattering intensities for θ-(BEDT-TTF)₂CsZn(SCN)₄ with various external currents applied along the c-axis direction at 12 K. The intensity is plotted as a function of k (along the b^* direction) in units of the reciprocal lattice constant. There are two diffuse streaks at $q_1 = (2/3, k, 1/3)$ and $q_2 = (0, k, 1/2)$ corresponding to charge order domains with different patterns. Figures 5a and b show the intensities at $q_2 + G_2$ and $q_1 + G_1$, respectively, where $G_1 = (2, 1, 1)$ and $G_2 = (3, 1, 0)$ are reciprocal lattice vectors chosen suitably for the measurement conditions. Whereas the $q_2 + G_2$ streak has a finite interlayer correlation, the $q_1 + G_1$ streak does not.

B2. With increasing temperature, the negative derivative resistance rapidly fades away, although the nonlinear resistance survives up to higher temperatures. At low temperatures, charge-ordered domains begin to appear. We expect the charge order to be characterized by a constant energy gap Δ, although the phase may have no long-range order. Then the charge transport should be of activation-type with an activation energy $-\Delta$. To include the giant nonlinear conduction effect, we allow Δ to be dependent on I_{ex}, and propose the following phenomenological expression:

$$V_{sample}/I_{ex} = R_{CO}\exp[\Delta_{I_{ex}}/k_B T] + R_N \qquad (1)$$

where R_{CO} and R_N are the resistances for the charge-ordered and conducting electrons, respectively. At low temperatures, we can safely neglect R_N and the temperature dependence of $\Delta_{I_{ex}}$. Then V_{sample}/I_{ex} plotted on a logarithmic scale as a function of $1/T$ gives $\Delta_{I_{ex}}$, as shown in Fig. 4. The data show an upward curve, which is consistent with the temperature dependence of the resistivity of the charge-density-wave material $K_{0.3}MoO_3$ (ref. 13). This arises from a rapid growth of the gap $\Delta_{I_{ex}}$ below 20 K, and the temperature-independent $\Delta_{I_{ex}}$—that is, $\Delta(I_{ex}, T) = \Delta(I_{ex}, 0)$—is only valid for $T \ll 20$ K. We focused on the I_{ex} dependence of $\Delta_{I_{ex}}$ at 4 K, so we evaluated the magnitude of $\Delta_{I_{ex}}$ by fitting the data close to 4 K with the solid lines indicated in Fig. 4. Note that the slope, which is equal to $\Delta_{I_{ex}}/k_B$, decreases with increasing I_{ex}.

The value of Δ extracted from such analysis is plotted as a function of I_{ex} in the inset of Fig. 4. Δ/k_B for $I_{ex} \to 0$ is 13 K. This value is close to the temperature $T = 20$ K below which the resistivity rapidly increases (a signature of the growth of the charge order), thus validating to some extent our evaluation of Δ. It should be emphasized that Δ decreases roughly linearly with increasing I_{ex}, suggesting that the external current rapidly suppresses the charge order. Accordingly, negative derivative resistance can occur when the suppression of $\exp[\Delta/k_B T]$ is so rapid that $I_{ex}\exp[\Delta/k_B T]$ becomes a decreasing function of I_{ex}.

We note the following. (1) The negative derivative resistance was observed also in the in-plane (c-axis) direction. Thus, the voltage–current characteristics discussed here are not an interlayer effect. (2)

Second column (page 524)

Essentially identical voltage–current characteristics were observed in θ-(BEDT-TTF)₂CsZn(SCN)₄ along the b- and c-axis directions, which are therefore inherent to the Cs salt. Some samples showed a similar a.c. oscillation from d.c. input. (3) The measurements in (1) and (2) above were done in a four-probe configuration with a pulse current source, which indicates that the intrinsic thyristor effects are free from the contact resistance and heating effects.

Finally, to clarify the melting of the charge order by external currents, we show diffraction data under different applied currents. For the experimental requirements, we used θ-(BEDT-TTF)₂CsZn(SCN)₄ with the external current applied along the c direction. Figure 5 shows d.c. current dependence of the diffuse scattering intensities at $q_1 = (2/3, k, 1/3)$ and $q_2 = (0, k, 1/2)$ at 12 K, which correspond to different charge order domains competing with each other. The intensity was 1,000 times weaker than that of the lattice Bragg reflection, so we used a four-circled diffractometer (wavelength $\lambda = 0.083$ nm) and synchrotron radiation as an X-ray source at BL02B1/SPring-8, Japan (details in the legend to Fig. 5). As is clearly shown, q_2 loses its intensity with increasing current, while q_1 remains nearly intact. The external current suppresses mainly the charge ordering with the q_2 modulation that is responsible for the insulating behaviour, consistent with the current-dependent Δ in Fig. 4.

1. Streetman, B. G. Solid State Electronic Devices 2nd edn, Ch. 11 (Prentice-Hall, Englewood Cliffs, 1980).
2. Mori, H., Tanaka, S. & Mori, T. Systematic study of the electronic state in θ-type BEDT-TTF organic conductors by changing the electronic correlation. Phys. Rev. B 57, 12023–12029 (1998).
3. Seo, H. Charge ordering in organic ET compounds. J. Phys. Soc. Jpn 69, 805–820 (2000).
4. Clay, R. T., Mazumdar, S. & Campbell, D. K. Charge ordering in θ-(BEDT-TTF)₂X materials. J. Phys. Soc. Jpn 71, 1816–1819 (2002).
5. Nogami, Y. et al. Structural modulation in θ-(BEDT-TTF)₂CsM'(SCN)₄ (M' = Co, Zn). Synth. Met. 103, 1911 (1999).
6. Watanabe, M., Nogami, Y., Oshima, K., Mori, H. & Tanaka, S. Novel pressure-induced 2k_F CDW state in organic low-dimensional compound θ-(BEDT-TTF)₂CsCo(SCN)₄. J. Phys. Soc. Jpn 68, 2654–2663 (1999).
7. Mori, T. Non-stripe charge order in the θ-phase organic conductors. J. Phys. Soc. Jpn 72, 1469–1475 (2003).
8. Nishio, Y. et al. Specific heat and metal-insulator transition of (BEDT-TTF)₂M2n(SCN)₄ (M = Cs, Rb). Synth. Met. 103, 1905–1906 (1999).
9. Takahashi, T. et al. Charge ordering in non-dimerized BEDT-TTF based organic conductors. ¹³C-NMR experiments. Phys. IV Fr. 12(Pr9), 201–204 (2002).
10. Inagaki, K., Terasaki, I., Mori, H. & Mori, T. Large dielectric constant and giant nonlinear conduction in the organic conductor θ-(BEDT-TTF)₂Cs2n(SCN)₄. J. Phys. Soc. Jpn 73, 3364–3369 (2004).
11. Maeda, A., Notomi, M., Uchinokura, K. & Tanaka, S. Evidence for the existence of the inherent periodicity in the switched state at low temperatures in K₀.₃MoO₃. Phys. Rev. B 36, 7709–7711 (1987).
12. Gunn, J. B. Microwave oscillations of current in III–V semiconductors. Solid State Commun. 1, 88–91 (1963).
13. Gruner, G. Density Waves in Solids 56–57 (Addison-Wesley, Reading, Massachusetts, 1994).

Right page (page 525)

Optical isotropy and iridescence in a smectic 'blue phase'

Jun Yamamoto[1,2]†, Isa Nishiyama[1], Miyoshi Inoue[1] & Hiroshi Yokoyama[1,2]

When liquid crystal molecules are chiral, the twisted structure competes with spatially uniform liquid crystalline orders, resulting in a variety of modulated liquid crystal phases, such as the cholesteric blue phase[1], twist grain boundary[2–4] and smectic blue phases[5]. Here we report a liquid crystal smectic blue phase (SmBP$_{Iso}$), formed from a two-component mixture containing a chiral monomer and a 'twin' containing two repeat units of the first molecule connected by a linear hydrocarbon spacer. The phase exhibits the simultaneous presence of finite local-order parameters of helices and smectic layers, without any discontinuity on a mesoscopic length scale. The anomalous softening of elasticity due to a strong reduction in entropy caused by mixing the monomer and the twin permits the seamless coexistence of these two competing liquid crystal orders. The new phase spontaneously exhibits an optically isotropic but uniformly iridescent colour and automatically acquires spherical symmetry, so that the associated photonic band gap[6–9] maintains the same symmetry despite the local liquid crystalline order. We expect a range of unusual optical transmission properties based on this three-dimensional isotropic structure, and complete tunability due to the intrinsic softness and responsiveness of the liquid crystalline order against external fields.

We have designed a two-component mixture that consists of a chiral monomer (3B1M7) and its twin (BMHBOP-6)[10]. The twin consists of two equivalent monomer units connected by a linear hydrocarbon spacer, as shown in Fig. 1. We termed it a 'commensurate' mixture because the length of the twin is exactly twice that of the monomer. We found that mixing the twin into monomer is apparently equivalent to the introduction of connecting chains between two monomers, which freeze the motion of the monomers. There are two concentrations—ϕ_m and ϕ_c—that are equivalent to the concentrations of the monomer and (R,R) enantiomer in the twin component, respectively.

We note that six modulated phases appear in the mixture, as shown in the phase diagram (Fig. 1), but only the isotropic liquid (Iso) and smectic-A (S$_A$) phases appear in a pure monomer. We identified three different SmBPs—SmBP$_{X1}$, SmBP$_{X2}$ and SmBP$_{X3}$. They appear to be similar to the previously reported phases SmBP$_1$, SmBP$_2$ and SmBP$_3$, respectively[5]. We also identified a fourth smectic blue phase, SmBP$_{Iso}$. A characteristic feature of SmBP$_{Iso}$ is that it exhibits a completely uniform colour under a polarizing microscope without any type of macroscopic pattern or texture. Moreover, the colour does not change when the sample is rotated in any direction. This proves that SmBP$_{Iso}$ has a completely isotropic optical property. It should be noted that SmBP$_{Iso}$ can be detected only within a very narrow range of ϕ_m, from 0.65 to 0.75. SmBP$_{X1}$ and SmBP$_{X2}$ can be distinguished clearly from SmBP$_{Iso}$ by their characteristic platelet textures, as shown in Fig. 2a and b, respectively.

During the cooling process, SmBP$_{Iso}$ appeared below 127 °C and was identified by the appearance of a uniform iridescent colour, as shown in Fig. 2b. The wavelength of the colour increased with a decrease in the temperature, which is a unique feature independent of both ϕ_m and ϕ_c. The platelet texture of SmBP$_{X2}$ appeared below 124 °C. During the reversible heating process, the platelet texture spontaneously melted above 124 °C, which is the temperature at which the uniform colour disappeared during the cooling process, into the uniformly coloured texture of SmBP$_{Iso}$. The temperature dependence of the colour of SmBP$_{Iso}$ was identical for both the cooling and heating processes, and no hysteresis was observed.

Thus, Fig. 2b provides two crucial experimental results. First, all phases (SmBP$_{X3}$, SmBP$_{Iso}$ and SmBP$_{X2}$) can be proved to be thermal equilibrium phases because these three phase transitions—SmBP$_{X3}$ to SmBP$_{Iso}$ and SmBP$_{Iso}$ to SmBP$_{X2}$—were confirmed to be thermodynamically reversible. Second, the isotropic nature of SmBP$_{Iso}$ arises from an inherent feature of its internal structure, and it is not related to the existence of a polycrystalline structure during the dynamical process of phase transition. The phase transition (and colour change) is quite smooth and rapid without any time delay during the nucleation or crystal-growth processes.

Spectroscopy experiments with polarized visible light revealed that both the optical rotatory power and transmitted light intensity of the linearly polarized light in SmBP$_{Iso}$ exhibited a large wavelength
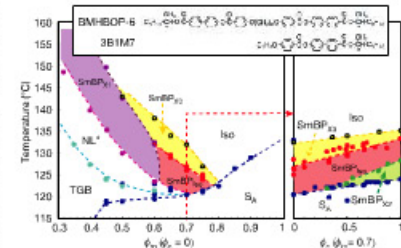

Figure 1 | Phase diagram for the twin/monomer mixture. Left, the monomer concentration (ϕ_m) dependence; right, the optical purity (ϕ_c) dependence of the twin by fixing $\phi_m = 0.7$. The TGB and N1* phases can be easily be identified under a polarizing microscope because of their large optical anisotropy and characteristic patterns. The inset shows the molecular formulas of the twin (BMHBOP-6) and monomer (3B1M7).

[1]ERATO Yokoyama Nano-structured Liquid Crystal Project, JST, 5-9-9 Tokodai, Tsukuba 300-2635, Japan. [2]Nanotechnology Research Institute, AIST, 1-1-1 Umezono, Tsukuba 305-8568, Japan. †Present address: Department of Physics, Graduate School of Science, Kyoto University, Kitashirakawa, Sakyo, Kyoto 606-8502, Japan.

dependence, as shown in Fig. 3a. The spectrum did not change when the sample was rotated in any direction, which again confirmed the isotropic optical property. From the following results, we can conclude that the colour originates from the spatial distribution of a helix, which is similar to that of the cholesteric (Ch) phase. (1) In the short-wavelength region, the optical rotatory power diverges and an extremely small amount of light is transmitted. The short-wavelength region is similar to the pitch band of selective reflection, which is commonly observed in the Ch phase. (2) The short-wavelength cut-off is independent of the sample thickness d, whereas the reflectivity increases only with an increase in d. (3) The transmittance of circularly polarized light is completely dependent on the optical handedness of the mixture.

Thus, these results confirm the existence of the helix and its isotropic distribution in space. Moreover, the transmittance of light at a greater wavelength, far from the band edge, is close to unity even in the case of an extremely thick sample (~1 mm), which indicates the absence of any domain structure with a length scale greater than the helix pitch. During the X-ray experiment, only one broad scattering peak was observed in the small angle region. This is a direct confirmation that all six modulated phases—twist grain boundary (TGB), chiral line nematic (NL*), SmBP$_{X1}$, SmBP$_{X2}$, SmBP$_{X3}$ and SmBP$_{Iso}$—have a finite smectic order with the exception of the order parameter difference. As shown in Fig. 3b, the peak intensity begins to grow continuously from SmBP$_{X3}$ to the S$_A$ phase. The characteristic length derived from the peak position is smoothly connected to the layer repeat distance of S$_A$ in all the other phases. Thus, we can identify only the Iso to SmBP$_{X3}$ phase transition in the X-ray results. In contrast, all the modulated phases are clearly distinguished by their macroscopic viscoelastic properties[11], as shown in Fig. 4a. In SmBP$_{X3}$, viscoelastic relaxation appears and a frequency-dependent real part is observed; however, the fluidity

remains constant. We note that a frequency-independent finite real part appears in SmBP$_{Iso}$. The static elasticity of SmBP$_{Iso}$ is approximately one order smaller than the layer compression modulus of S$_A$.

The most important and unusual characteristics of SmBP$_{Iso}$ are that it spontaneously exhibits an optically isotropic but uniformly iridescent colour. X-ray and visco-elastic measurements clearly demonstrate that all SmBPs have a smectic order, and the simultaneous existence of the helices is confirmed from the optical rotatory power. Thus, two different types of liquid crystalline orders coexist in space with frustration in all SmBPs. A universal feature is that spontaneous symmetry breaking leads to a liquid crystalline order, which results in the appearance of spatial macroscopic anisotropy. However, the spherical symmetry only can be restored spontaneously by randomizing the regular spatial distribution of both the liquid crystalline orders on a larger scale in SmBP$_{Iso}$. The texture of SmBP$_{Iso}$ is clearly smooth and homogeneous without any discontinuity. If a system has a true isotropic symmetry, spatial uniformity is automatically realized without any internal domain
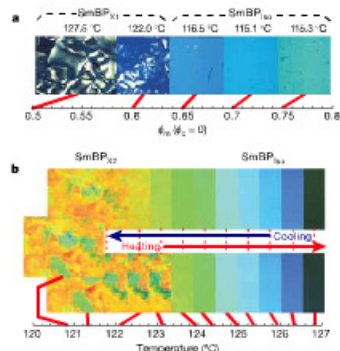
structures. This implies that the symmetry of the novel SmBP$_{Iso}$ is intrinsically spherical.

To establish the details of the internal structure of SmBP$_{Iso}$ we first note that both the layer compression modulus B and Frank elastic constant K_1 in the S$_A$ phase are minimized at approximately $\phi_m = 0.7$, as shown in Fig. 4b. At this value of ϕ_m, the value of B is 20 times smaller, while that of K_1 is almost two orders of magnitude smaller than their values in the pure-monomer system. By comparing Fig. 1 and Fig. 4b, we observe that SmBP$_{Iso}$ was stabilized only within a very narrow concentration range in which a drastic softening of B and K_1 occurs. SmBP$_{Iso}$ certainly results from the anomalous

Figure 2 | Polarizing microscope photographs in SmBPs. a, ϕ_m dependence of the patterns of SmBP$_{X3}$ and SmBP$_{Iso}$ by fixing the optical purity of the twin ($\phi_c = 0$). Red bars indicate the concentration of the mixture. A characteristic platelet texture of the SmBP$_{X3}$ phase was observed below $\phi_m = 0.6$. The SmBP$_{Iso}$ texture was observed to be of uniform colour from $\phi_m = 0.65–0.75$. **b**, Temperature dependence of the patterns during both the cooling and heating processes of the SmBP$_{Iso}$ to SmBP$_{X2}$ phase transition. Red bars indicate the actual temperature of the sample. A sample ($\phi_m = 0.7$ and $\phi_c = 1$) was introduced in a 1-mm-thick quartz cell. The thermo-reversible SmBP$_{Iso}$ to SmBP$_{X2}$ phase transition is clearly identified at approximately 124 °C.
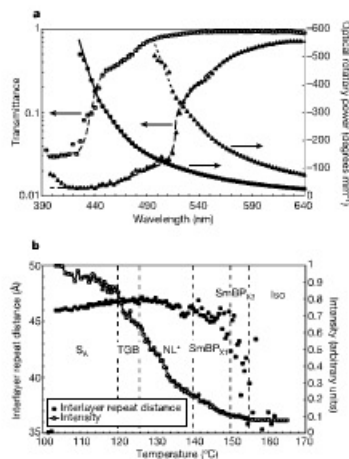

Figure 3 | Macroscopic and microscopic structural analysis in SmBPs. a, Transmittance (open circles) and optical rotatory power (closed circles) of SmBP$_{Iso}$ ($T = 124.7$ °C) deduced from the analyser angle dependence of the spectrum of the polarized visible light ($\phi_m = 0.7$, $\phi_c = 1$). The transmittance decreases by less than 2% in the short-wavelength region below 430 nm whereas there is complete transparency above 600 nm. The optical rotatory power also diverges in the short-wavelength region, which is similar to the pitch band of selective reflection in the cholesteric phase. It is remarkable that the edge of the pitch band continuously shifted to 530 nm for the supercooled SmBP$_{Iso}$ ($T = 120.2$ °C), as indicated by the triangular symbols (open and closed symbols represent the transmittance and optical rotatory power, respectively). **b**, Temperature dependence of the smectic order measured by X-ray scattering obtained from a sample ($\phi_m = 0.45$, $\phi_c = 0$). Only one scattering peak was detected in the small-angle region below 156 °C, which confirms that with the exception of the Iso phase, all the phases have a finite local smectic order. The intensity of the scattering peak increases continuously from SmBP$_{X3}$ to S$_A$, as indicated by the open circles. The characteristic length is smoothly connected to the layer repeat distance of S$_A$, as indicated by the filled circles.
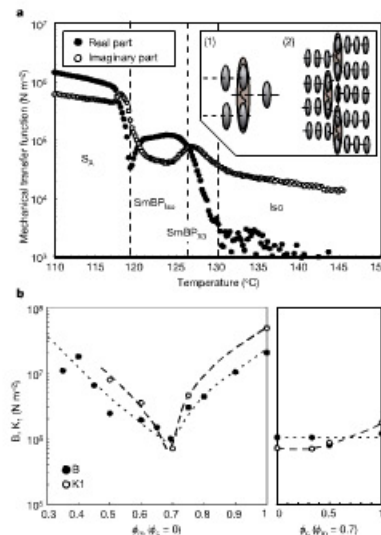

Figure 4 | Mechanical properties in SmBPs. a, Temperature dependence of the real (filled circles) and imaginary (open circles) parts of the complex mechanical transfer function of the sample ($\phi_m = 0.7$, $\phi_c = 0$) at 200 Hz. Both the SmBP$_{X3}$ and SmBP$_{Iso}$ phases can be observed. It is evident that the finite static elastic part observed in the SmBP$_{X3}$ phase is one order of magnitude smaller than the layer compression modulus of the S$_A$ phase. The small value of the real part in the SmBP$_{X3}$ phase is due to the viscoelastic relaxation. The insets show a schematic representation of the molecular models: (1) There are two energy minima with respect to the relative position of the monomer and twin. The position of the dotted line corresponds to the stable position based on the entropic origin. The centre of gravity of the twin and monomer, namely the centre of the fluctuation motion, should be settled on the centre of the layers. On the other hand, the position of the dotted line corresponds to the lateral interaction of the local intermolecular interaction. The chemical contrast could be enhanced by the commensurability of the system. Each position was shifted merely by half the monomer length. (2) A defect can be induced easily in the layer by the localization of the twin molecules. **b**, ϕ_m and ϕ_c dependencies of the layer compression modulus B (red dots) and Frank elastic constant K_1 (blue circles) in the S$_A$ phase. Our viscoelastic measurement can simultaneously determine B and K_1 by detecting the dynamic change in B immediately after the application of a large step-like dilative strain.

softening of the smectic layer. Using this information, we propose a rough sketch of the molecular model, as shown in inset (1) of Fig. 4a. There are two energy minima with respect to the relative position of the monomer and twin. First, the centre of gravity of all the molecules must lie on the mid-plane of the smectic layer, owing to the requirement of fluctuation motion. This is completely equivalent to our concept of molecular cooling of the twin molecules. Second, another local energy minimum is due to the local molecular interactions. We emphasize that the commensurability of our mixture could enhance the effect of the lateral interaction. Thus, we can assume that a continuous slip of the smectic layer can easily be generated by the localization of the twin without decreasing the defect core energy, as shown in inset (2) of Fig. 4a.

As is evident in the freeze-fracture replica and frozen replica of the free air interface of TEM photographs of SmBP$_{Iso}$ (see Supplementary Figs 1, 2 and 3), we found a random and continuous interconnected sponge-like structure in SmBP$_{Iso}$. The characteristic size of this structure exhibits a large dispersion around the visible light wavelength. A multiple stack of the smectic layers in the interconnected structure is also shown in Supplementary Figs 2 and 3. A multi-lamellar interconnected cubic structure was recently proposed theoretically[12]; however, the proposed structure has spatial regularity because it is a model of the optically cubic crystals of SmBP$_{X1}$ and SmBP$_{X2}$. In fact, these SmBPs exhibit angle-dependent selective reflection owing to the regular spatial arrangement of the helices, which appears to be identical to the double helix structure in ChBPs. Therefore, the lattice of the multi-lamellar interconnected structure must coexist and be frustrated with the lattice of the double helices.

Thus we can consider that the frustration induces the melting of the lattice of the multi-lamellar interconnected structure in a manner related to the liquid crystal microemulsion[13]. A random sponge-like distribution is then produced, which is similar to the well-known cubic-sponge phase transition of the unilamellar interconnected structure in the lyotropic system. We conclude that SmBP$_{Iso}$ is the multi-lamellar sponge phase. Furthermore, the SmBP$_{X2}$ to SmBP$_{Iso}$ transition can be attributed to the newly discovered multi-lamellar cubic-sponge phase transition. Neither of the liquid crystalline orders, that is the smectic layer or the helix, disappear during these phase transitions. The multi-lamellar interconnected units are also maintained in both phases, and only their spatial regularity is lost in SmBP$_{Iso}$.

Theoretical calculations of the driving force of the multi-lamellar interconnected structure[13] considered only the gaussian curvature energy without chiral interaction. However, our system is extremely sensitive to optical purity. We suggest that the chirality promotes the generation of a negative gaussian curvature of the multilayer owing to the coupling between the chiral interaction and layer deformation. Another theoretical work predicted that the bending of the layer should be induced by molecular chirality[14,15]. The behaviour of the B$_4$ phase in the original banana molecules[16] is similar to that of SmBPs. However, a clear mosaic texture and weak birefringence are always observed in the B$_4$ phase under a polarizing microscope[17]. These characteristics completely contradict the spherical symmetry of SmBP$_{Iso}$. On the other hand, the banana and twin (dimmer) molecules have a similar molecular structure. As compared to the bilayer membrane formed by the molecules with strong steric incompatibility between the head and tail, it is reasonable that the smectic layer, which consists of the banana or twin molecules, should prefer the saddle-splay deformation of the layers, which is a common fundamental unit for all SmBPs, not only for SmBP$_{Iso}$.

In summary, we have experimentally found a novel smectic phase SmBP$_{Iso}$ which is optically isotropic, has true spherical symmetry and exhibits iridescent colour. However, the distribution of the helix in the multi-lamellar interconnected structure is still unclear. It is highly advantageous that the characteristic length of the system can be completely tuned in the visible light wavelength by external factors such as temperature and light irradiation. This is because the

photonic bandgap is formed by a self-organized hierarchical structure driven by the frustration in the soft liquid crystalline order. Until now, such tunability has not been achieved even by using photonic crystal materials that were fabricated well. In fact, a similar isotropic medium has been designed by modelling the complete randomness in polycrystalline domains. An artificial design for a self-organized hierarchical structure must be compatible with bottom-up 'nanotechnology' to use the frustration induced by impurities in the liquid crystalline orders[13]. These long-range elastic interactions can stabilize huge structures such as biological systems in which short-range molecular interactions become completely irrelevant.

1. Kelzerow, H. S. & Bahr, C. (eds) *Chirality in Liquid Crystals* 186–222 (Springer, New York, 2002).
2. Renn, S. R. & Lubensky, T. C. Abrikosov dislocation lattice in a model of the cholesteric-to-smectic A transition. *Phys. Rev. A.* 38, 2132–2147 (1988).
3. Goodby, J. W. *et al.* Characterization of a new helical smectic liquid crystal. *Nature* 337, 449–452 (1989).
4. Dierking, I. & Lagerwall, S. T. A review of textures of TGB* phase under different anchoring conditions. *Liq. Cryst.* 26, 83–95 (1999).
5. Pansu, B., Grelet, E., Li, M. H. & Nguyen, H. T. Hexagonal symmetry for smectic blue phases. *Phys. Rev. E* 62, 658–665 (2000).
6. John, S. Electromagnetic absorption in a disordered medium near photon mobility edge. *Phys. Rev. Lett.* 53, 2169–2172 (1984).
7. Yablonovitch, E. Inhibited spontaneous emission in solid-state physics and electronics. *Phys. Rev. Lett.* 58, 2059–2062 (1987).
8. John, S. Strong localization of photons in certain disordered dielectric superlattices. *Phys. Rev. Lett.* 58, 2486–2489 (1987).
9. Busch, K. & John, S. Liquid-crystal photonic-band-gap materials: the tunable electromagnetic vacuum. *Phys. Rev. Lett.* 83, 967–970 (1999).
10. Nishiyama, I., Yamamoto, J., Goodby, J. W. & Yokoyama, H. Symmetric chiral liquid crystalline twin exhibiting stable ferroelectric and antiferroelectric phases and a chirality-induced isotropic-isotropic liquid transition. *J. Mater. Chem.* 11, 2690–2693 (2001).
11. Yamamoto, J. & Okano, K. Anomalous hydrodynamic behaviors of smectic liquid crystals at low frequencies. *Jpn. J. Appl. Phys.* 30, 754–763 (1991).
12. DiDonna, B. A. & Kamien, R. D. Smectic phases with cubic symmetry: the splay analog of the blue phase. *Phys. Rev. Lett.* 89, 215504 (2002).
13. Yamamoto, J. & Tanaka, H. Transparent nematic phase in liquid-crystal based microemulsion. *Nature* 409, 321–325 (2001).
14. MacKintosh, F. C. & Lubensky, T. C. Orientational order, topology, and vesicle shapes. *Phys. Rev. Lett.* 67, 1169–1173 (1991).
15. Zhong-can, O. & Ji-xing, L. Helical structure of tilted chiral lipid bilayers viewed as cholesteric liquid crystals. *Phys. Rev. Lett.* 65, 1679–1682 (1990).
16. Nori, T., Sekine, T., Watanabe, J., Furukawa, T. & Takezoe, H. Distinct ferroelectric smectic liquid crystals consisting of banana shaped achiral molecules. *J. Mater. Chem.* 6, 1231–1233 (1996).
17. Thisayukta, J., Takezoe, H. & Watanabe, J. Study on helical structure of the B₄ phase formed from achiral banana-shaped molecules. *Jpn. J. Appl. Phys.* 40, 3277–3287 (2001).

LETTERS

Europe-wide reduction in primary productivity caused by the heat and drought in 2003

Ph. Ciais[1], M. Reichstein[2,3], N. Viovy[1], A. Granier[4], J. Ogée[5], V. Allard[6], M. Aubinet[7], N. Buchmann[8], Chr. Bernhofer[9], A. Carrara[10], F. Chevallier[1], N. De Noblet[1], A. D. Friend[1], P. Friedlingstein[1], T. Grünwald[9], B. Heinesch[7], P. Keronen[11], A. Knohl[12,13], G. Krinner[14], D. Loustau[5], G. Manca[2]†, G. Matteucci[15]†, F. Miglietta[16], J. M. Ourcival[17], D. Papale[2], K. Pilegaard[18], S. Rambal[17], G. Seufert[15], J. F. Soussana[6], M. J. Sanz[10], E. D. Schulze[12], T. Vesala[11] & R. Valentini[2]

Future climate warming is expected to enhance plant growth in temperate ecosystems and to increase carbon sequestration[1,2]. But although severe regional heatwaves may become more frequent in a changing climate[3,4], their impact on terrestrial carbon cycling is unclear. Here we report measurements of ecosystem carbon dioxide fluxes, remotely sensed radiation absorbed by plants, and country-level crop yields taken during the European heatwave in 2003. We use a terrestrial biosphere simulation model[5] to assess continental-scale changes in primary productivity during 2003, and their consequences for the net carbon balance. We estimate a 30 per cent reduction in gross primary productivity over Europe, which resulted in a strong anomalous net source of carbon dioxide ($0.5\,Pg\,C\,yr^{-1}$) to the atmosphere and reversed the effect of four years of net ecosystem carbon sequestration[6]. Our results suggest that productivity reduction in eastern and western Europe can be explained by rainfall deficit and extreme summer heat, respectively. We also find that ecosystem respiration decreased together with gross primary productivity, rather than accelerating with the temperature rise. Model results, corroborated by historical records of crop yields, suggest that such a reduction in Europe's primary productivity is unprecedented during the last century. An increase in future drought events could turn temperate ecosystems into carbon sources, contributing to positive carbon-climate feedbacks already anticipated in the tropics and at high latitudes[1,2].

Europe experienced a particularly extreme climate anomaly during 2003, with July temperatures up to 6 °C above long-term means, and annual precipitation deficits up to 300 mm yr⁻¹, 50% below the average. The presence of an extensive network of instrumentation for the monitoring of ecosystem fluxes at this time, with continuous records of CO_2, water, and energy fluxes[5,6], helped us to assess the impact of such an extreme event on the continental-scale carbon balance. We analysed CO_2 fluxes from 14 forest sites and one grassland site for 2002–2003 (Table 1). Flux records are generally not yet long enough to provide long-term average references, and therefore we used 2002 as a reference (see Methods). Hourly fluxes of photosynthesis (gross primary productivity, GPP) and total

ecosystem respiration (TER) are separated from CO_2 net fluxes (net ecosystem exchange, NEE), using the same method for each site[7].

Given inter-site differences in drought duration and intensity, soil characteristics, vegetation state, and species-specific responses to climate variation, one would not expect a uniform response of GPP to the abnormal conditions of 2003. Yet, Table 1 (also Supplementary Fig. S1) clearly shows that nearly all sites experienced a significant GPP reduction in 2003. The GPP drop coincides with reduced evapotranspiration and soil drying due to the rainfall deficit (Supplementary Fig. S1). Generally, below a threshold of −0.4 in relative extractable water, water stress occurs, causing both GPP and transpiration to decrease in response to stomatal closure[10,11]. Particularly large reductions in GPP were found in temperate deciduous beech and northern Mediterranean forests (Hesse, Hainich, Roccarespampani, San Rossore), together with reductions in canopy conductance (in 2003, conductance reached only 15% of its 2002 value at Hesse). These productive temperate and Mediterranean forests were greatly affected by extreme drought and/or heat (Fig. 1). Moreover, the GPP did not entirely recover from the summer stress during the remainder of the growing season (Fig. 1). Southern evergreen forest sites El Saler (pine) and Puéchabon (oak) also experienced a reduction in GPP during the heatwave (Table 1). Southern forest sites with an herbaceous layer that normally dries in summer were less affected by the heatwave and drought (Pianosa).

Warmer temperatures are expected to increase both microbial and plant respiration. However, during the 2003 summer, TER fell in parallel with GPP at most sites (Table 1, Supplementary Fig. S1). A reduction in both plant respiration (due to diminished substrates) and microbial soil respiration (also due to drought) can explain such parallel TER and GPP responses. Possible artefacts of the method used to separate gross fluxes[8] can largely be ruled out because of the close correlation between the independent quantities TER and mid-day NEE, the latter dominated by GPP (Fig. 1). Overall, those forests where GPP strongly decreased also had reduced net carbon uptake (NEE), with Hesse and Tharandt even temporarily becoming net

[1]Laboratoire des Sciences du Climat et de l'Environnement, LSCE, F-91191, Gif sur Yvette, France. [2]Department of Forest Environment and Resources, DISAFRI, University of Tuscia, I-01100 Viterbo, Italy. [3]Potsdam Institute for Climate Impact Research, Telegrafenberg C4, D-14473 Potsdam, Germany. [4]Ecologie et Ecophysiologie Forestières, Centre de Nancy, F-54280 Champenoux, France. [5]Functional Ecology and Environmental Physics, Ephyse, INRA, F-33612 Villenave d'Ornon, France. [6]Grassland Ecosystem Research, INRA, 234 Avenue du Brézet, Clermont-Ferrand, F-63039, France. [7]Institute of Plant Sciences, Universitätsstrasse 2, ETH Zentrum LFW C56, CH-8092 Zuerich, Switzerland. [8]Faculté des Sciences Agronomiques, Avenue de la Faculté d'Agronomie 8, B-5030 Gembloux, Belgium. [9]Department of Meteorology, Institute of Hydrology and Meteorology, Technische Universität Dresden, D-01062 Dresden, Germany. [10]Fundacion CEAM C/ Charles Darwin, Parque Tecnologico de Paterna, E-46980 Valencia, Spain. [11]Department of Physical Sciences, University of Helsinki PO-Box 64, Finland. [12]Max-Planck Institute for Biogeochemistry, Postfach 10 01 64, D-07701 Jena, Germany. [13]Department of Environmental Science Policy and Management, Ecosystem Science Division, University of California, Berkeley, California 94720, USA. [14]Laboratoire de Glaciologie et Géophysique de l'Environnement, 54 rue Molière, F-38402, Saint Martin d'Hères, France. [15]Institute for Environment and Sustainability, Joint Research Center European Commission, TP 280, I-21020 Ispra, Italy. [16]IBIMET-CNR, Ple delle Cascine, 18, I-50144 Firenze, Italy. [17]Dream CEFE-CNRS, 1919 route de Mende, F-34293 Montpellier, France. [18]Biosystems Department, Risø National Laboratory, 4000 Roskilde, Denmark. †Present addresses: Centro di Ecologia Alpina, Viote del Monte Bondone, I-38040 Trento, Italy (G. Manca); ISAFOM-CNR, Via Cavour 4-6, I-87036, Rende, Italy (G. Matteucci).